Chinese Chemical Letters 34 (2023) 108196

Contents lists available at ScienceDirect

Chinese Chemical Letters

journal homepage: www.elsevier.com/locate/cclet

Dual-functional photocatalysis boosted by electrostatic assembly of porphyrinic metal-organic framework heterojunction composites with CdS quantum dots

Zhiyao Chen, Sihong Li, Qijie Mo, Li Zhang*, Cheng-Yong Su*

MOE Laboratory of Bioinorganic and Synthetic Chemistry, Lehn Institute of Functional Materials, School of Chemistry, Sun Yat-sen University, Guangzhou 510006, China

ARTICLE INFO

Article history:
Received 8 December 2022
Revised 8 January 2023
Accepted 5 February 2023
Available online 11 February 2023

Keywords:
Metal-organic framework composites
Electrostatic self-assembly
Dual-functional photocatalysis
CdS quantum dots
Metalloporphyrin

ABSTRACT

Photocatalytic dual-functional reaction under visible light irradiation represents a sustainable development strategy. In detail, H_2 production coupled with benzylamine oxidation can remarkably lower the cost by replacing sacrificial agents. In this work, CdS quantum dots (CdS QDs) were successfully loaded onto the surface of a porphyrinic metal-organic framework (Pd-PCN-222) by the electrostatic self-assembly at room temperature. The consequent Pd-PCN-222/CdS heterojunction composites displayed superb photocatalytic activity under visible light irradiation, achieving a H_2 production and benzylamine oxidation rate of 5069 and 3717 μmol g^{-1} h^{-1} with >99% selectivity in 3 h. There is no noticeable loss of catalytic capability during three successive runs. Mechanistic studies by *in situ* electron spin resonance and X-ray photoelectron spectroscopy disclosed that CdS QDs injected photoexcited electrons to Pd-PCN-222 and then Zr_6 clusters under visible-light irradiation, and thus CdS QDs and Zr_6 clusters behave as the photocatalytic oxidation and reduction centers, respectively.

As carbon neutrality becomes a common goal for the whole world, scientists make an endeavor to develop clean energy to cut down the discharge of greenhouse gasses. As green energy, H_2 has gained extensive attraction thanks to clean-burning characterization and wide range of applications. Up to now, tremendous efforts have been made to exploit catalysts for H_2 generation driven by solar energy [1]. It is regarded as an ideal way to generate H_2 by photocatalytic water splitting. However, sacrificial agents such as lactic acid, triethanolamine and methanol are usually required due to the sluggish water-oxidation kinetics [2]. In order to lower the cost and swell the profit by utilizing photo-generated holes, selective organic synthesis have been chosen to couple with H_2 production, which also denoted as dual-functional cooperative photoredox system [3]. It is extremely ideal to simultaneously product H_2 and value-added chemicals with high selectivity and conversion [4–13]. Furthermore, gaseous H_2 and oxidation products can be naturally separated without extra operations, which also avoid the occurrence of reverse and side reaction. Among all, selective amine oxidation is one of the suitable reactions for this dual-functional system, which can be operated under mild conditions. As the oxidation products, imines or imidazoles can be applied in pharmaceutical, agricultural and synthetic chemistry.

Owing to suitable band position and relatively narrow band gap which result in decent visible light absorption, CdS quantum dots (CdS QDs) have been frequently selected for this reaction system, which has already shown impressive catalytic activity in H_2 evolution and selective organic transformations [14]. However, superfacial S^{2-} of CdS QDs can be oxidized by photogenerated holes, which seriously limits their stability and practical application as photocatalysts [15]. Doping CdS QDs with metal cations such as Fe^{2+}, Co^{2+} and Ni^{2+} [16], hybridizing with semiconductors such as TiO_2 [17], and compositing with porous metal-organic frameworks (MOFs) such as UiO-66 [18] and MIL-53 [19] are effective ways to enhance the stability and facilitate charge transfer and separation. Nevertheless, during the synthesis of CdS-based composites, abscission might occur due to high content of CdS loaded and weak interaction between CdS and support [20]. To solve the abscission problem, electrostatic self-assembly is an effective way, which not only facilitate electronic communication to enhance interaction but also provide considerable catalytic activities [21–24].

Porphyrinic metal-organic frameworks (PMOFs), which are based on visible light photosentisized porphyrin ligands, have

* Corresponding authors.
E-mail addresses: zhli99@mail.sysu.edu.cn (L. Zhang), cesscy@mail.sysu.edu.cn (C.-Y. Su).

https://doi.org/10.1016/j.cclet.2023.108196
1001-8417/

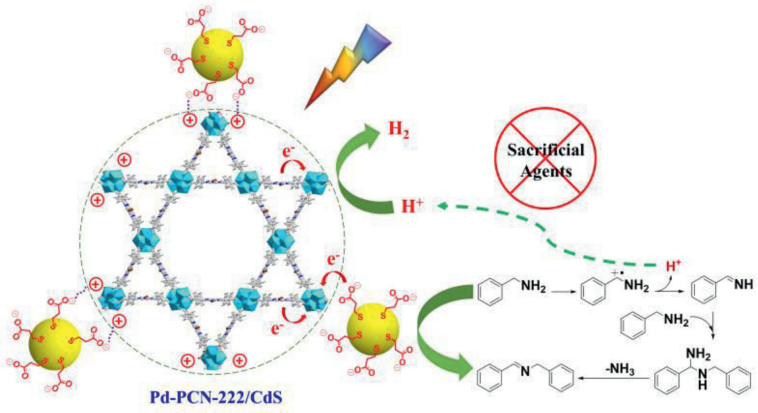

Fig. 1. The structures and catalytic behaviours of Pd-PCN-222/CdS.

emerged as powerful heterogeneous catalysts [25–28] and especially for photocatalytic reactions such as CO_2 reduction [29], hydrogen evolution reaction [30] and cross-dehydrogenative coupling reaction [31]. On account of the backdonation from the filled d_π orbital of the metal to the empty e_g (π^*) orbital of porphyrin, Group VIII (*e.g.*, Ru, Rh, Pd, Ir, and Pt) porphyrins are considered as desirable sensitizers with triplet yields close to 100% and rapid intersystem crossing (ISC) [32].

Herein we report the study of dual-functional photocatalysis by porphyrinic metal-organic framework heterojunction composites with CdS QDs (Pd-PCN-222/CdS), which were facilely synthesized by the electrostatic self-assembly at room temperature (Fig. 1). Zeta potentials of Pd-PCN-222 and CdS QDs at pH 7 were 9.6 mV and −37.5 mV, respectively, indicative of a robust electrostatic interaction in the composite. The assembly facilitated the electronic communication between Pd-PCN-222 and CdS QDs, leading to efficient and selective dual-functional reaction of hydrogen evolution and amine oxidation, with an unprecedented maximum H_2 and imine evolution rate of 5069 and 3717 μmol g^{-1} h^{-1} in 3 h, with >99% selectivity, respectively. No decrease was observed on the rate and selectivity after 3 runs. Further mechanistic studies by *in situ* electron spin resonance and X-ray photoelectron spectroscopy disclosed that CdS QDs injected photoexcited electrons to Pd-PCN-222 and then Zr_6 clusters under visible-light irradiation, and thus CdS QDs and Zr_6 clusters behave as the photocatalytic oxidation and reduction centers, respectively.

Pd-PCN-222 was synthesized by the self-assembly of Pd-TCPP and $ZrCl_4$ at 120 °C for 20 min, with an additional modulating reagent CF_3CO_2H. The bulk purity of Pd-PCN-222 was verified by powder X-ray diffraction (PXRD) patterns (Fig. S1 in Supporting information). Pd-PCN-222 had a *csq* topology composed by 3.7 nm diameter hexagonal and 1.3 nm diameter triangular channels as in PCN-222 [33], which also denoted as MOF-545 [34] and MMPF-6 [35]. On the other hand, 3-mercaptopropionic acid-modified CdS QDs, which were named after CdS-MPA, was prepared by a facile one-pot reaction of $CdCl_2$, MPA and Na_2S in water. The suspension of CdS-MPA in water showed the typical Tyndall effect when a red laser passed through it, indicative of the colloidal structures (Fig. S2 in Supporting information).

The composite of Pd-PCN-222/CdS was synthesized by the electrostatic self-assembly of Pd-PCN-222 and CdS-MPA at room temperature (Fig. 2). The capping molecule MPA could serve as both a stabilizer to disperse CdS QDs and a linker to combine CdS QDs and Pd-PCN-222 [36]. The *in situ* growth strategy of hydrothermal reaction at elevated temperature has been widely used to synthesize a variety of CdS-MOF materials such as CdS/UiO-66 [18], CdS/MIL-53(Fe) [19] and CdS@MOF-808 [37]. For comparison, electrostatic self-assembly at room temperature can minimize the negative effect caused by heat, which makes it possible for thermal instable MOFs to synthesize MOF/CdS composites. UV–vis spectroscopy of the supernatant of reaction solution disclosed that almost all soluble CdS QDs were firmly loaded on the external surfaces of Pd-PCN-222 (Fig. S3 in Supporting information).

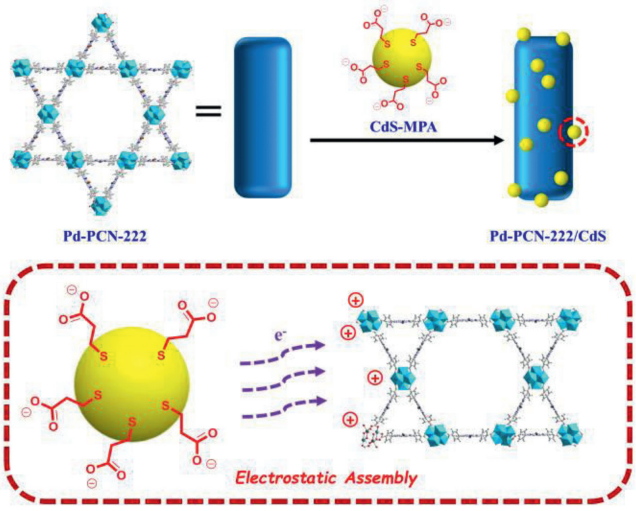

Fig. 2. Syntheses of Pd-PCN-222/CdS.

It is notable that upon the doping of CdS QDs, the crystallinity of both Pd-PCN-222 and CdS (JCPDS Card No. 41–1049) in the composite Pd-PCN-222/CdS remained (Fig. S4 in Supporting information). In addition, after the fresh samples of Pd-PCN-222/CdS were soaked in water, acetonitrile, and *N,N*-dimethylformamide (DMF) for 7 days, the crystallinity of the recycled samples was well kept by PXRD patterns, indicative of the strong chemical stability (Fig. S5 in Supporting information).

N_2 sorption experiments disclosed that the Brunauer-Emmett-Teller (BET) surface areas of Pd-PCN-222 and Pd-PCN-222/CdS were 2042 and 1326 m^2/g, respectively (Fig. S6a in Supporting information). This showed that the porosity of Pd-PCN-222 was well maintained after the loading of CdS QDs on the surface of Pd-PCN-222/CdS. The pore size distribution of Pd-PCN-222 and Pd-PCN-222/CdS was simulated by density function theory (DFT), disclosing that there were two types of pores, which was matched with the crystal structure of PCN-222 [33] and also proved that CdS QDs weren't incorporated into the pores (Fig. S6b in Supporting information).

Scanning electron microscopy (SEM) images revealed that Pd-PCN-222 was of rod-shape with about 500 nm in width and 2 μm

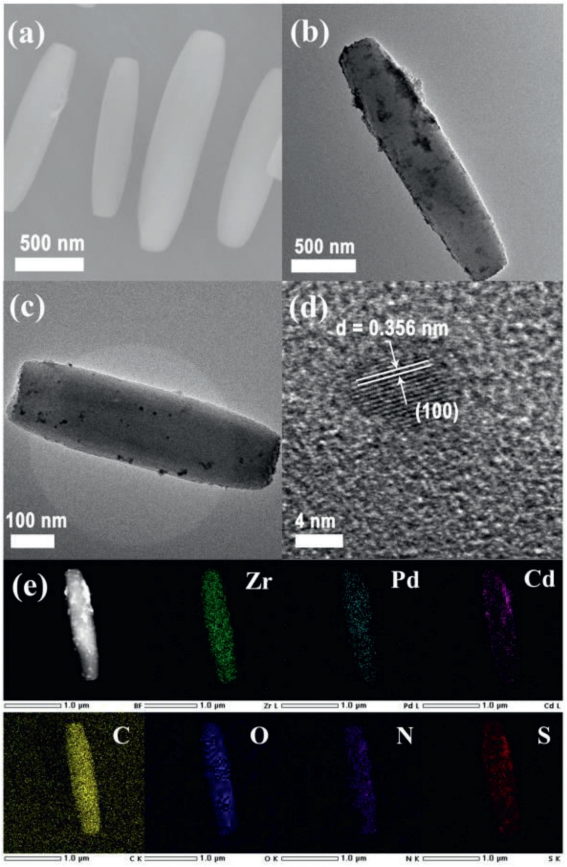

Fig. 3. SEM image of Pd-PCN-222 (a), TEM images of Pd-PCN-222/CdS(5.0) (b) and Pd-PCN-222/CdS(0.5) (c). The crystal lattice spacing of CdS in Pd-PCN-222/CdS(0.5) (d) and EDS images of Pd-PCN-222/CdS(5.0) (e).

in length (Fig. 3a). Transmission electron microscopy (TEM) patterns of Pd-PCN-222/CdS revealed that different content of CdS QDs were uniformly loaded on the external surfaces of Pd-PCN-222 (Figs. 3b and c). The crystal lattice spacing of CdS was 0.356 nm, which was corresponding to (100) of the nanocrystal (Fig. 3d). All of the elements were uniformly distributed in Pd-PCN-222/CdS, which was demonstrated by TEM-EDX (energy-dispersive X-ray spectroscopy) elemental mapping images (Fig. 3e).

The oxidation state of Pd, Zr, Cd and S in Pd-PCN-222/CdS and the interaction between Pd-PCN-222 and CdS QDs were examined by X-ray photoelectron spectroscopy (XPS) (Figs. S7–S9 in Supporting information). The $3d_{5/2}$ and $3d_{3/2}$ peaks with binding energies at 338.1 and 343.5 eV, respectively, clearly confirmed the +2 valence state of Pd. Similarly, +2 valence state of Cd and −2 valence state of S were proved by the binding energies at $3d_{5/2}$ (404.8 eV) and $3d_{3/2}$ (411.5 eV) of Cd(+2) together with $2p_{3/2}$ (161.3 eV) and $2p_{1/2}$ (162.2 eV) of S(−2). The Cd 3d ($3d_{5/2}$, 405.5; $3d_{3/2}$, 412.2 eV) and S 2p ($2p_{3/2}$, 161.9; $2p_{1/2}$, 163.3 eV) peaks shifted to higher binding energies upon the load of CdS QDs onto the surface of Pd-PCN-222, indicative of probable electron transfer from CdS QDs to Pd-PCN-222 (Fig. S10 in Supporting information).

The formation mechanism of Pd-PCN-222/CdS was studied. Zeta potentials of CdS QDs and Pd-PCN-222 at pH 7 were −37.5 mV and 9.6 mV, respectively, indicative of a robust interfacial interaction in the composite (Fig. S11 in Supporting Information) [38]. Besides, it was reported that the isoelectric point of PCN-222 appeared at pH 8, indicating that the MOF was cationic at pH 7 [22]. The cationic feature of Pd-PCN-222 at neutral conditions helped it to attract the anionic CdS QDs [39]. Therefore, the interactions between Pd-PCN-222 and CdS were rather strong.

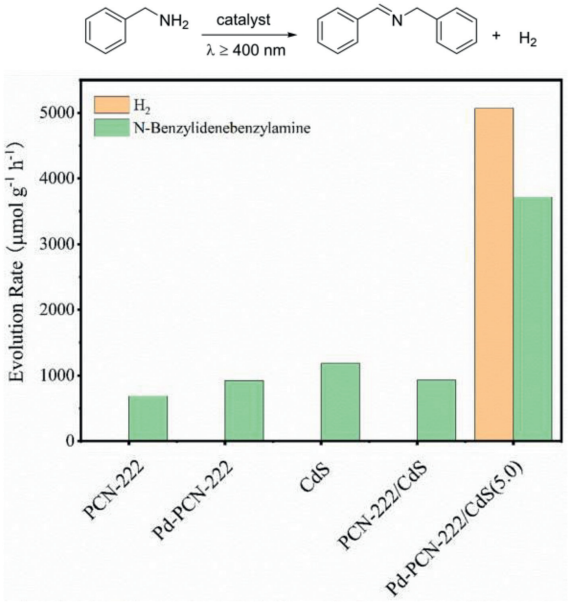

Fig. 4. Comparison of catalytic activities in the presence of different catalysts.

Measurements of light absorption range, band gap energies and HOMO/LUMO potentials of Pd-PCN-222, CdS QDs and Pd-PCN-222/CdS were taken in advance of the photocatalytic study. Pd-PCN-222 displayed powerful light absorption with Soret band (424 nm) and Q band (520 nm) while CdS QDs absorbed light until around 550 nm, as shown by solid UV–vis absorption spectroscopy. Upon the load of CdS QDs, the Soret band and Q band of Pd-PCN-222 remained, and meanwhile a new absorption peak around 590 nm appeared, which meant shrinkage of band gap and formation of type-II heterojunction (Fig. S12 in Supporting information).

Mott–Schottky (M–S) measurements were performed at 500, 1000 and 1500 Hz (Fig. S13 in Supporting information). Characteristics of n-type semiconductors were confirmed by the positive slopes of the M–S plots. The positions of conduction bands, whose values were equal to LUMO, were determined to be −0.47 V and −0.61 V (*vs.* NHE) for Pd-PCN-222 and CdS, respectively, from the intersections. The band gap energies (E_g) of Pd-PCN-222 and CdS were calculated to be 2.15 eV and 2.33 eV, respectively, by Tauc plots. Afterwards, based on E_g and conduction bands, their valence bands (equal to HOMO) were accordingly obtained (Fig. S14 in Supporting information). In regards to the hydrogen evolution (−0.42 V *vs.* NHE) and the benzylamine oxidation (+0.76 V *vs.* NHE), it was reasonable for the above materials to behave as photocatalysts for the dual-functional system due to more negative LUMO potentials than proton reduction and more positive HOMO potentials than benzylamine oxidation (Fig. S13 in Supporting information) [8,30].

Encouraged by strong visible light absorption and appropriate LUMO and HOMO potentials, the photocatalytic proton reduction coupled with benzylamine oxidation was carried out under atmospheric pressure, room temperature and visible light irradiation ($\lambda \geq 400$ nm). Catalytic results in the presence of pristine PCN-222, Pd-PCN-222, CdS QDs, PCN-222/CdS and Pd-PCN-222/CdS were shown in Fig. 4. It could be seen that none of the pristine PCN-222, Pd-PCN-222 and CdS QDs could promote the reaction, but only Pd-PCN-222/CdS possessed excellent activity, in which the H_2 and *N*-benzylidenebenzylamine evolution rates were up to 5069 and 3717 μmol g^{-1} h^{-1}, respectively, after 3 h irradiation (Table S1, entries 1–4 and 9 in Supporting information).

Subsequently, Pd-PCN-222/CdS(n) with different weight ratios, where n means that the weight ratio of Pd-PCN-222 and CdS is

10:n, were tested under the same condition, in which a volcano tendency was observed (Fig. S15 and Table S1, entries 5–10 in Supporting information). Inductively coupled plasma mass spectrometry (ICP-MS) confirmed the actual mass ratio of CdS in Pd-PCN-222/CdS(n) (n = 0.5, 1.0, 3.0, 4.0, 5.0, 6.0) are 4.2%, 7.0%, 22.3%, 27.5%, 35.5% and 49.3%, respectively. Pd-PCN-222/CdS exhibited the highest catalytic activity when the weight ratio of Pd-PCN-222 to CdS was 10:5. The loading of CdS QDs on the surface of Pd-PCN-222 could accelerate the charge transfer and electron–hole separation and make the photocatalytic reaction easier. However, an excessive amount of CdS might block the channel of Pd-PCN-222 and prevent it from harvesting visible light. This might explain the volcano tendency.

Blank experiments revealed that light irradiation and photocatalyst were essential for the reaction (Table S2 in Supporting information). The reaction scope regarding benzylamines was evaluated using Pd-PCN-222/CdS(5.0) as the catalyst (Table S3 in Supporting information). It was found that benzylamines with different *para*-substituents performed smoothly to give the corresponding oxidation products with a yield up to 99% (Fig. S16 and Table S3 in Supporting information).

Furthermore, Pd-PCN-222/CdS displayed stable catalytic performances in three consecutive recycling runs (Fig. S17 and Table S4 in Supporting information). TEM images, PXRD patterns and XPS spectra of the recycled Pd-PCN-222/CdS revealed that the morphology, crystallinity and the element valences remained after the catalytic reactions (Figs. S18–S20 in Supporting information). The leached amounts of Pd and Cd from Pd-PCN-222/CdS into the reaction solution were determined to be around 0.11% and 0.03%, respectively, through ICP-OES analysis.

The catalytic performances of Pd-PCN-222/CdS were further compared with the reported MOF and MOF composites (Table S5 in Supporting information). For example, Co-MIX and Pt/PCN-777 gave a H_2 evolution rate of 564 and 332 μmol g^{-1} h^{-1}, respectively [8,9]. In consideration of better adsorption of visible light and suitable oxidation ability for transformation of organic compounds, metal sulfates were deposited in stable MOFs to get Ni_5CdS@MIL-101 and $CdIn_2S_4$@MIL-53-$SO_3Ni_{1/2}$, which gave rise to a H_2 evolution rate of 9800 and 850 μmol g^{-1} h^1, respectively [10,11]. In a word, Pd-PCN-222/CdS exhibited a particularly efficient dual-functional photocatalyst among MOF composites with superior H_2 evolution rate, oxidation rate, selectivity and catalytic durability.

Ultrafast transient absorption (TA) spectroscopy was examined to study the electron–hole separation efficiency. TA spectra were measured under 400 nm for the effective excitation of porphyrinic MOFs. As for Pd-PCN-222 and Pd-PCN-222/CdS, a positive excited-state absorption (ESA) signal was observed at 507 nm and 510 nm, respectively, and a negative ground-state bleaching (GSB) signal was detected at 454 nm (Figs. S21a and b in Supporting information). The recovery exhibited a two-exponential decay manner, that is, τ_1 = 12,300 ps (59.0%) and τ_2 = 685 ps (41.0%) for Pd-PCN-222, and τ_1 = 1000 ps (67.7%) and τ_2 = 20,000 ps (32.3%) for Pd-PCN-222/CdS (Table S6 in Supporting information). The lifetime of τ_1, which was caused by the trapped electrons of surface states, was largely decreased in Pd-PCN-222/CdS, indicative of a faster charge transfer at the interface between CdS and Pd-PCN-222. Meanwhile, Pd-PCN-222/CdS displayed a much longer lifetime of τ_2, which should be attributed to the longer exciton relaxation process in Pd-PCN-222/CdS due to effective spatial separation. Pd-PCN-222/CdS showed accelerated TA kinetics compared with Pd-PCN-222 (Fig. S21c in Supporting information).

Photophysical performances were tested by steady-state photoluminescence (PL) spectroscopy (Fig. S22 in Supporting information). Upon excitation at 455 nm, the PL emission intensity of Pd-PCN-222/CdS was dramatically decreased relative to Pd-PCN-222,

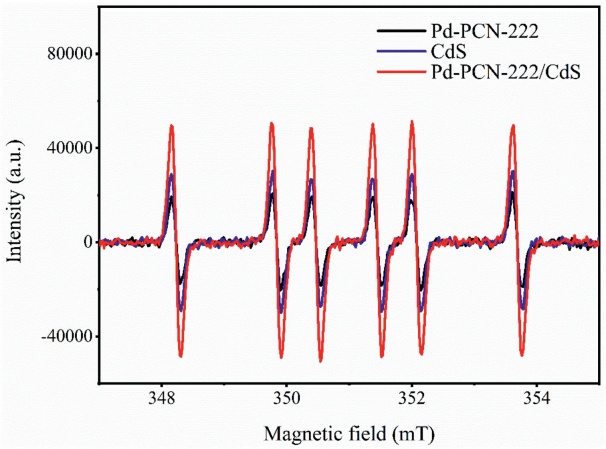

Fig. 5. *In situ* EPR spectra of Pd-PCN-222/CdS under illumination in the presence of benzylamine and DMPO in anhydrous acetonitrile under N_2 atmosphere.

indicating that the carrier recombination was evidently inhibited after loading the CdS QDs on the surface of Pd-PCN-222. The time-resolved fluorescence decay spectra of Pd-PCN-222 and Pd-PCN-222/CdS at 298 K under vacuum disclosed that their PL lifetimes were 530.3 μs and 47.9 μs, respectively (Fig. S23 and Table S7 in Supporting information). The remarkably long-lived triplet states were competent for electron transfer of Pd-PCN-222 and Pd-PCN-222/CdS.

The charge-separation efficiency was further measured by photocurrent response and electrochemical impedance spectroscopy (EIS). Compared to those of pristine Pd-PCN-222, stronger photocurrent response and smaller EIS radius of Pd-PCN-222/CdS indicated less recombination of photogenerated electrons and holes and faster interfacial charge transfer (Figs. S24 and S25 in Supporting information). Surface photovoltage spectra (SPV) were collected to gain evidence of interfacial electric field (Fig. S26 in Supporting information). Compared to pristine Pd-PCN-222 and CdS QDs, the Pd-PCN-222/CdS composites showed significantly stronger SPV signals, demonstrating that a more efficient charge separation existed [40]. Positive signals further confirmed that both Pd-PCN-222 and CdS were n-type semiconductors.

To demonstrate the photocatalytic mechanism, *in situ* electron spin resonance (ESR) spectra have been studied. First of all, light-induced porphyrin π-cation radical was monitored at 140 K under air atmosphere. Only porphyrin radical cation can be detected under air atmosphere, since signals of Zr^{3+} would be quenched by oxygen. As shown by the ESR light-dark difference spectra, Pd-PCN-222/CdS gave a much enhanced porphyrin π-cation radical signal at g = 2.0036 than pristine Pd-PCN-222 upon light irradiation, indicated that the generation of photogenerated radicals could be accelerated by the loading of CdS QDs (Fig. S27 in Supporting information) [41].

Secondly, ligand-to-cluster charge transfer (LCCT) process in Pd-PCN-222 was monitored at 140 K in the presence of TEOA in anhydrous acetonitrile under N_2 atmosphere. The significantly enhanced ESR signal at g = 2.001 can be ascribed to electron-trapped Zr-oxo clusters, indicating electrons transfer from the Pd-porphyrin ligand during photocatalysis (Fig. S28 in Supporting information) [29]. As for Pd-PCN-222/CdS, the EPR signal of Zr^{3+} further strengthened after the loading of CdS, which suggested that the photogenerated electrons might transfer from CdS QDs to Pd porphyrin and then to Zr-oxo clusters [42]. Nonetheless, the photogenerated electrons might also transfer from CdS QDs directly to Zr-oxo clusters.

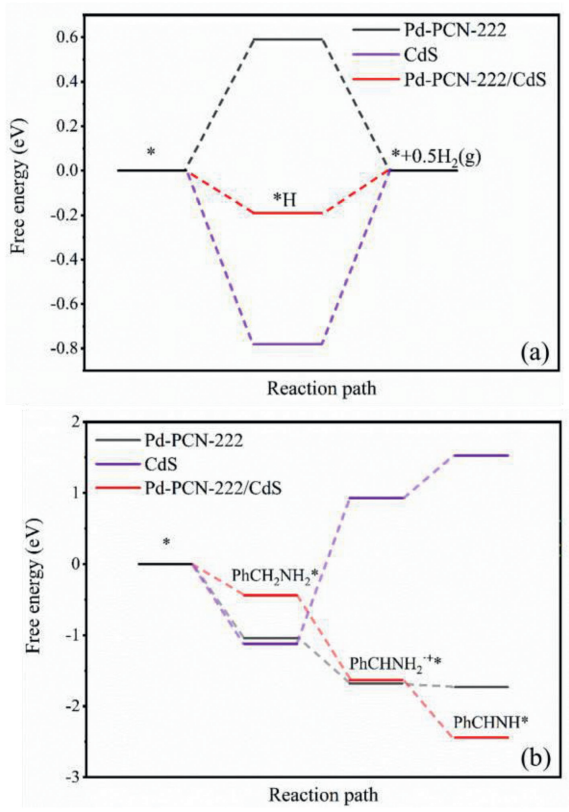

Fig. 6. The calculated energy profile for hydrogen production (a) and benzylamine dehydrogenation (b) of CdS, Pd-PCN-222 and Pd-PCN-222/CdS.

The effect of CdS QDs in the photocatalytic dehydrogenative coupling of benzylamine was tested by *in situ* ESR in the presence of 5,5-dimethyl-1-pyrroline *N*-oxide (DMPO) as a spin-trapping reagent. No radical species were observed under dark (Fig. 5 and Fig. S29 in Supporting information). The C-centered α-amine radical was gradually evolved upon irradiation and subsequently trapped by DMPO, which was confirmed by the 1:1:1:1:1:1 pattern ($\alpha_N = 16.1$, $\alpha_H = 22.5$) [43]. This suggested that Pd-PCN-222, CdS QDs and Pd-PCN-222/CdS could initiate amines' deprotonation by their photogenerated holes.

To reveal the interfacial charge transfer pathway between CdS and Pd-PCN-222, *in situ* XPS was performed (Fig. S30 in Supporting information). Upon visible-light irradiation for 20 min, there was a slightly negative shift in the Zr 3d binding energy, suggesting an increase in the electron density on the Zr_6 clusters of Pd-PCN-222. Meanwhile, a slightly positive shift can also be observed in Pd 3d, indicating a decrease in the electron density on the Pd-porphyrin. The binding energy of Cd 3d remained stable upon visible-light irradiation, but still higher than that of pristine CdS. Combined with binding energy shifts of normal XPS of Cd 3d and S 2p of CdS QDs and Pd-PCN-222 CdS QDs, charge carrier migration pathway across the Pd-PCN-222/CdS interface could be confirmed [44,45]. In other words, type-II heterojunction was formed between Pd-PCN-222 and CdS QDs, and the CdS QDs injected excited electrons into Pd-PCN-222 under visible-light irradiation, while Pd-TCPP injecting excited electrons into Zr_6 clusters through LCCT process, which was in good agreement with the electron injection mechanism and EPR results.

The reaction mechanism was unveiled by density functional theory (DFT) calculations. As mentioned above, Pd-PCN-222 and CdS were proposed to be the active sites of H_2 production and benzylamine oxidation, respectively. The catalytic activity for the hydrogen evolution was usually evaluated by Gibbs free energy of hydrogen adsorption (ΔG_{H^*}). The energy barriers of H_2 production of pristine Pd-PCN-222 and Pd-PCN-222/CdS were calculated to be 0.59 eV and −0.19 eV, respectively (Fig. 6a). The lower energy barrier of Pd-PCN-222/CdS assisted in its more effective H_2 production reaction, which was in accordance with the experimental results.

In addition, the bond cleavage process of C_α–H over pristine Pd-PCN-222, CdS and Pd-PCN-222/CdS was shown in Fig. 6b. Initially, benzylamine was adsorbed on the surface of the catalyst and to form the $PhCH_2NH_2^{+\bullet}$. The adsorption energies of benzylamine on Pd-PCN-222, CdS and Pd-PCN-222/CdS were −1.04, −1.12 and −0.44 eV, respectively. Then, H^+ was dissociated from the adsorbed $PhCH_2NH_2^{+\bullet}$ and to form $Ph\dot{C}HNH_2$ radical and PhCH=NH imine. The energy barrier of C_α–H cleavage over the interface of Pd-PCN-222, CdS and Pd-PCN-222/CdS were −0.64, 2.03 and −1.19 eV, implying that Pd-PCN-222/CdS was the most efficient for the oxidation of benzylamine. This imine could couple with another benzylamine to give the target product (Fig. S31 in Supporting information). Therefore, the heterojunction between Pd-PCN-222 and CdS could lower the energy barriers of both reduction and oxidation process.

In summary, a new MOF composite Pd-PCN-222/CdS was prepared by the electrostatic self-assembly of positively charged Pd-PCN-222 and negatively charged CdS QDs at room temperature. Pd-PCN-222/CdS displayed strong stability and superb photocatalytic activity in dual-functional reaction including hydrogen evolution and amine oxidation under visible light irradiation. The remarkable reaction activity of Pd-PCN-222/CdS for simultaneous H_2 evolution and benzylamine oxidation could be summarized by three aspects. Firstly, Pd-PCN-222/CdS was synthesized by electrostatic self-assembly of Pd-PCN-222 and CdS-MPA at room temperature, which facilitated the formation of heterojunction. Secondly, the heterojunction accelerated the charge transfer and electron–hole separation. Thirdly, the charge transfer made CdS-MPA and Pd-PCN-222 easier for oxidation and reduction reaction, respectively. Further work about the design of porphyrinic MOF composites with heterojunction and their photocatalytic applications is on the process.

Declaration of competing interest

The authors declare that they have no known competing financial interests or personal relationships that could have appeared to influence the work reported in this paper.

Acknowledgments

The authors acknowledge support from the National Natural Science Foundation of China (Nos. 21773314, 21821003 and 21890382), the Guangdong Natural Science Funds for Distinguished Young Scholar (No. 2019B151502017).

Supplementary materials

Supplementary material associated with this article can be found, in the online version, at doi:10.1016/j.cclet.2023.108196.

References

[1] S. Liu, C. Zhang, Y. Sun, et al., Coord. Chem. Rev. 413 (2020) 213266.
[2] Q. Wang, K. Domen, Chem. Rev. 120 (2020) 919–985.
[3] M.Y. Qi, M. Conte, M. Anpo, et al., Chem. Rev. 121 (2021) 13051–13085.
[4] Y. Huang, C. Liu, M. Li, et al., ACS Catal. 10 (2020) 3904–3910.
[5] P. Wang, S. Fan, X. Li, et al., Nano Energy 89 (2021) 106349.
[6] P. She, J.S. Qin, J. Sheng, et al., Small 18 (2022) 2105114.
[7] W. Yu, D. Zhang, X. Guo, et al., Catal. Sci. Technol. 8 (2018) 5148–5154.
[8] H. Liu, C. Xu, D. Li, H.L. Jiang, Angew. Chem. Int. Ed. 57 (2018) 5379–5383.
[9] M. Klarner, S. Hammon, S. Feulner, et al., ChemCatChem 12 (2020) 4593–4599.

[10] H. Li, Y. Yang, X. Jing, et al., Chem. Asian J. 16 (2021) 1237–1244.
[11] H.H. Zhang, G.P. Zhan, Z.K. Liu, C.D. Wu, Chem. Asian J. 16 (2021) 1499–1506.
[12] Q. Xiao, S. Sarina, E.R. Waclawik, et al., ACS Catal. 6 (2016) 1744–1753.
[13] K. Chen, W. Zhang, Y. Bai, et al., Chin. Chem. Lett. 34 (2023) 107319.
[14] J.Y. Li, Y.H. Li, M.Y. Qi, et al., ACS Catal. 10 (2020) 6262–6280.
[15] Y. Liu, D. Huang, M. Cheng, et al., Coord. Chem. Rev. 409 (2020) 213220.
[16] J. Wang, T. Xia, L. Wang, et al., Angew. Chem. Int. Ed. 57 (2018) 16447–16451.
[17] M.Y. Qi, Q. Lin, Z.R. Tang, Y.J. Xu, Appl. Catal. B: Environ. 307 (2022) 121158.
[18] H.Q. Xu, S. Yang, X. Ma, et al., ACS Catal. 8 (2018) 11615–11621.
[19] P. Li, X. Yan, S. Gao, R. Cao, Chem. Eng. J. 421 (2021) 129870.
[20] K. Yang, Z. Yang, C. Zhang, et al., Chem. Eng. J. 418 (2021) 129344.
[21] Q.Q. Bi, J.W. Wang, J.X. Lv, et al., ACS Catal. 8 (2018) 11815–11821.
[22] G. Paille, M. Gomez-Mingot, C. Roch-Marchal, et al., J. Am. Chem. Soc. 140 (2018) 3613–3618.
[23] Y. Dong, Q. Hu, B. Li, et al., Appl. Catal. B: Environ. 304 (2022) 120998.
[24] N.Y. Huang, H. He, S. Liu, et al., J. Am. Chem. Soc. 143 (2021) 17424–17430.
[25] J. Liu, Y.Z. Fan, K. Zhang, et al., J. Am. Chem. Soc. 142 (2020) 14548–14556.
[26] Y. Wang, H. Cui, Z.W. Wei, et al., Chem. Sci. 8 (2017) 775–780.
[27] C. Chen, Q. Mo, J. Fu, et al., ACS Catal. 12 (2022) 3604–3614.
[28] Z. Liang, H. Guo, H. Lei, R. Cao, Chin. Chem. Lett. 33 (2022) 3999–4002.
[29] J. Liu, Y.Z. Fan, X. Li, et al., Appl. Catal. B: Environ. 231 (2018) 173–181.
[30] S. Li, H.M. Mei, S.L. Yao, et al., Chem. Sci. 10 (2019) 10577–10585.
[31] S. Li, J. Wang, L. Dong, et al., Chin. Chem. Lett. 34 (2023) 107633.
[32] A. Antipas, M. Gouterman, J. Am. Chem. Soc. 105 (1983) 4896–4901.
[33] D. Feng, Z.Y. Gu, J.R. Li, et al., Angew. Chem. Int. Ed. 51 (2012) 10307–10310.
[34] W. Morris, B. Volosskiy, S. Demir, et al., Inorg. Chem. 51 (2012) 6443–6445.
[35] Y. Chen, T. Hoang, S. Ma, Inorg. Chem. 51 (2012) 12600–12602.
[36] H. Li, W.Y. Shih, W.H. Shih, Ind. Eng. Chem. Res. 46 (2007) 2013–2019.
[37] K. Gao, H. Li, Q. Meng, et al., ACS Appl. Mater. Interfaces 13 (2021) 2779–2787.
[38] M.Y. Qi, Y.H. Li, M. Anpo, et al., ACS Catal. 10 (2020) 14327–14335.
[39] J. Jing, J. Yang, W. Li, et al., Adv. Mater. 34 (2022) 2106807.
[40] C. Zhang, C. Xie, Y. Gao, et al., Angew. Chem. Int. Ed. 61 (2022) e202204108.
[41] C. Xu, H. Liu, D. Li, et al., Chem. Sci. 9 (2018) 3152–3158.
[42] H. Li, F. Qin, Z. Yang, et al., J. Am. Chem. Soc. 139 (2017) 3513–3521.
[43] L. Wang, X.J. Wei, W.L. Jia, et al., Org. Lett. 16 (2014) 5842–5845.
[44] J. Low, B. Dai, T. Tong, et al., Adv. Mater. 31 (2019) 1802981.
[45] M. Zhang, M. Lu, Z.L. Lang, et al., Angew. Chem. Int. Ed. 59 (2020) 6500–6506.